



Microstructural Characteristics and Tensile Behavior of a Hot-Rolled Medium-Mn Steel (0.25C-8.5Mn-0.5Si-2.5Al) Processed by Intercritical Annealing Treatment

Yongjian Zhang, JiaoJiao Wang, Zhiqi Xie, Xiaoli Zhao, and Weijun Hui

(Submitted September 23, 2019; in revised form February 4, 2020; published online April 8, 2020)

Microstructural characteristics and tensile behavior of a novel hot-rolled medium-Mn steel, 0.25C-8.5Mn-0.5Si-2.5Al (wt.%), under different intercritical annealing temperatures (T_{IA}) were evaluated. The results show that an ultrafine duplex lamellar microstructure with a maximum volume fraction of retained austenite (RA) of 65 vol.% was obtained at T_{IA} of 750 °C. It was found that both the stability of the RA and its stability range play critical role in controlling the sustainable TRIP effect. The product of ultimate tensile strength and total elongation as high as ~ 66 GPa% was obtained at T_{IA} of 725 °C, which is much higher than those of previously investigated medium-Mn steels with similar Mn contents, indicating a great potential for the tested steel. The analysis of the fracture surface revealed that the steel exhibited a kind of micro-delamination fracture, which was found to be primarily nucleated at the interfaces of the transformation-induced martensite and ferrite, and the micro-delamination fracture became more significant with increasing T_{IA} .

Keywords intercritical annealing, mechanical property, medium-Mn steel, microstructures, TRIP effect

1. Introduction

Due to an ever-increasing demand for simultaneous improvement of vehicles for fuel efficiency and crashworthiness in the modern automobile industry, great efforts have been paid toward the research and development of advanced high-strength steels (AHSSs) over the past several decades (Ref 1). In general, AHSSs can be classified into three categories, namely the first-, second- and third-generation AHSSs (Ref 2-5). In comparison with the first- and second-generation AHSSs, the third-generation AHSSs exhibit intermediate properties and a better tradeoff between mechanical properties and material cost (Ref 3). The target combination of strength and ductility, i.e., the product of ultimate tensile strength (UTS) and total elongation (TEL), UTS \times TEL, is higher than ~ 30 GPa% for the third-generation AHSSs (Ref 4).

As one of the most potential candidates for the third-generation AHSSs, medium-Mn steel has attracted growing interest in the last decade due to its excellent combination of strength and ductility, as well as relatively low material cost and industrial feasibility (Ref 2-4). This superior mechanical property is primarily derived from a considerable fraction of

retained austenite (RA) and its transformation-induced plasticity (TRIP) effect during the deformation process (Ref 6-14). The Mn content in conventional low-alloyed TRIP steels, which are generally characterized by RA fraction lower than ~ 15 vol.% and UTS \times TEL of $\sim 15 \pm 10$ GPa%, is usually lower than 2.5 wt.% (Ref 15). As a strong austenite stabilizer, both thermodynamic calculation and experimental results have confirmed that the addition of Mn can result in a stable austenite equilibrium at room temperature due to strong Mn partitioning during intercritical annealing (IA) treatment in the ferrite + austenite region (Ref 2, 16, 17). Earlier work of Miller firstly reported that a RA fraction up to ~ 30 vol.% and thus a UTS of 878 MPa and a TEL of 34% were obtained in a 0.11C-5.7Mn (wt.%) steel (Ref 18). In recent years, many researchers have obtained RA fractions up to ~ 20 -60 vol.% and UTS \times TEL higher than 30 GPa% mainly depending on IA parameters and/or Mn content (Ref 2-19). Therefore, it is suggested that superior mechanical properties might be obtained to increase Mn content up to ~ 10 wt.% to further increase the RA fraction (Ref 3, 8). In fact, a summary of the mechanical properties of recently developed medium-Mn steels revealed that UTS \times TEL tends to increase with increasing Mn content (Ref 20).

More recently, Al has also been considered as a necessary alloy element in designing medium-Mn steels, although several problems related to steel casting process and surface quality should be further explored (Ref 2, 3, 6-9, 15). As a strong ferrite stabilizer, Al suppresses the cementite formation in a manner similar to that of Si. It was also found that the Al alloying of medium-Mn steels permits a higher IA temperature (T_{IA}) because the addition of Al increases the equilibrium transformation start (A_{e1}) and finish (A_{e3}) temperatures, and thus has a beneficial effect on significantly promoting the IA process (Ref 3, 21, 22). Moreover, the addition of Al to medium-Mn steels can lower the density of steel (Ref 23). Si is

Yongjian Zhang, JiaoJiao Wang, Zhiqi Xie, Xiaoli Zhao, and Weijun Hui, Materials Science and Engineering Research Center, School of Mechanical, Electronic and Control Engineering, Beijing Jiaotong University, Beijing 100044, People's Republic of China. Contact e-mail: zhangyongjian@bjtu.edu.cn.

an essential element in conventional TRIP steels; Si has the additional role of solid solution strengthening and high strain hardening rate of the ferrite phase by suppressing cross-slip, in contrast to Al (Ref 3, 24). Thus, a suitable addition of Si is still needed in designing medium-Mn steels.

There have already been several investigations concerning the microstructural evolution and mechanical properties of medium-Mn steels; however, more systematic studies are still helpful to further enhance the mechanical properties. Thus, in this study, a novel medium-Mn steel with a nominal composition of 0.25C-8.5Mn-0.5Si-2.5Al (wt.%) was prepared to study its microstructural evolution and mechanical properties at different T_{1A} after hot-rolling.

Table 1 Chemical composition (wt.%) and critical temperatures (°C) of the tested medium-Mn steel

C	Si	Mn	P	S	Al	A_{e1}	A_{e3}
0.25	0.54	8.67	0.004	0.004	2.69	645	830

2. Experimental Procedures

The chemical composition of the tested steel is listed in Table 1. Compared to our previous study based on 0.20C-5Mn-0.6Si-3Al (wt.%) (Ref 6), the C and Mn contents especially the latter were adjusted based on phase diagram calculations using the Thermo-Calc software for the purpose of obtaining comparable RA fraction after IA treatment. The A_{e1} and A_{e3} of the tested steel calculated by the Thermo-Calc software are also listed in Table 1. The steel was melted in laboratory vacuum-induction furnace and cast into a 110-kg steel ingot. After homogenization treatment at 1220 °C for 2 h, the ingot was hot-forged into plates of 30 mm thickness and then air-cooled to room temperature. The forged plates were soaked at 1200 °C for 2 h, hot-rolled to 5-mm-thick sheets and finally air-cooled. The hot-rolled sheets were then intercritically annealed using an electric resistance furnace at temperatures of 650, 675, 700, 725, 750, 775 and 800 °C with a duration of 1 h (henceforth named as the HR650, HR675, HR700, HR725, HR750, HR775 and HR800 samples, respectively).

The microstructures of the samples were observed using a scanning electron microscope (SEM) and transmission electron microscope (TEM) with an energy-dispersive x-ray spectrometer (EDS). The SEM samples were etched in a 2 vol.% nital solution after standard metallography sample preparation. The TEM thin foils were prepared in a twin-jet electropolishing

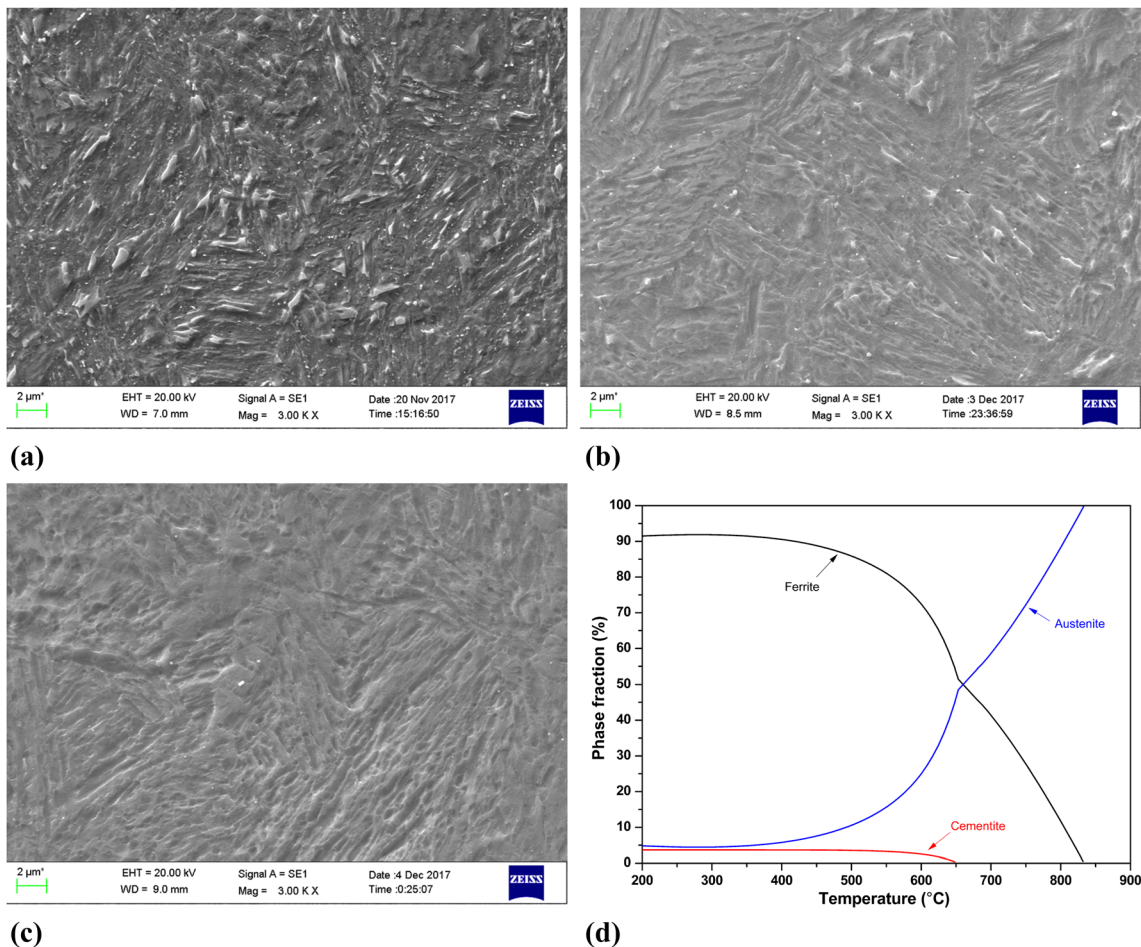


Fig. 1 SEM micrographs of the (a) HR650, (b) HR725 and (c) HR800 samples and (d) the phase volume fractions based on an equilibrium thermodynamic analysis predicted by Thermo-Calc and the TCFE8 database

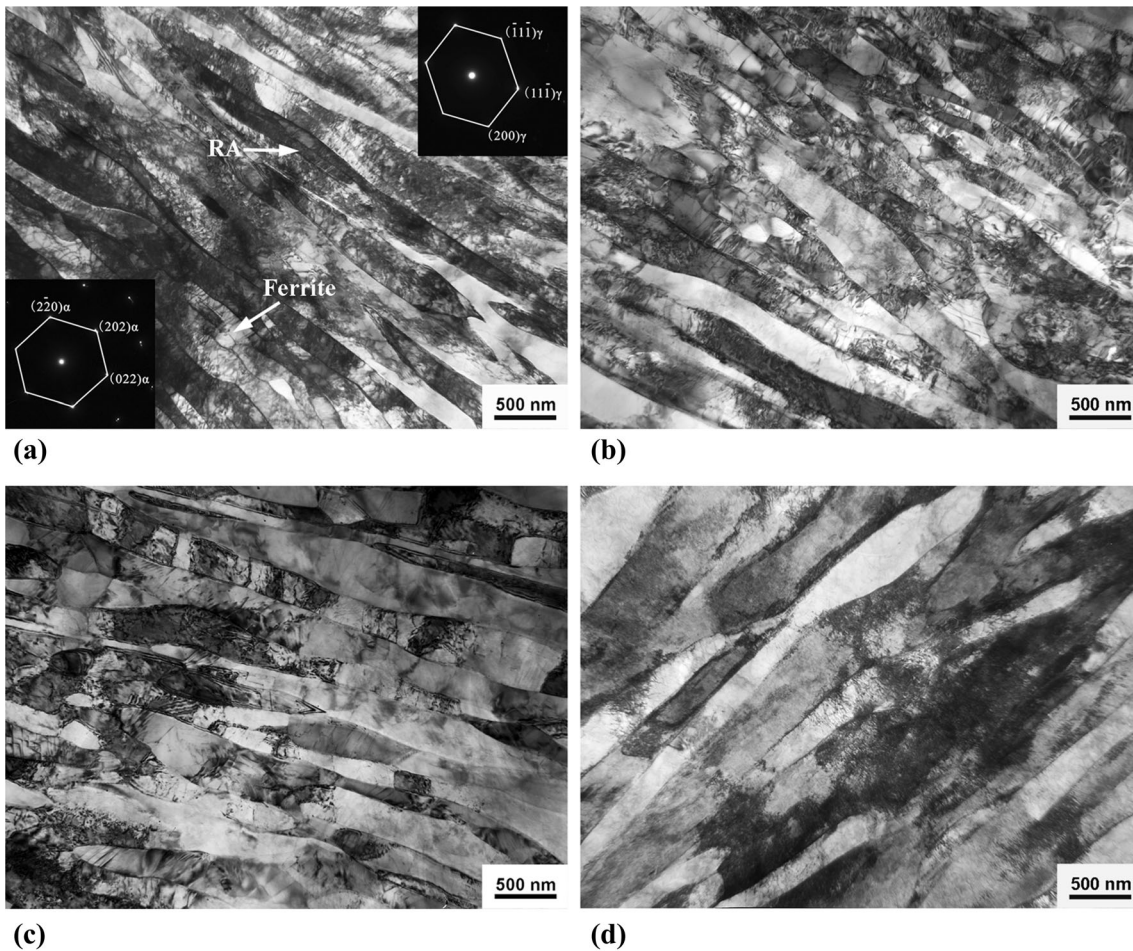


Fig. 2 TEM micrographs of the (a) HR650, (b) HR725, (c) HR750 and (d) HR800 samples [insets: selected area electron diffraction patterns of the lathy RA and ferrite in (a)]

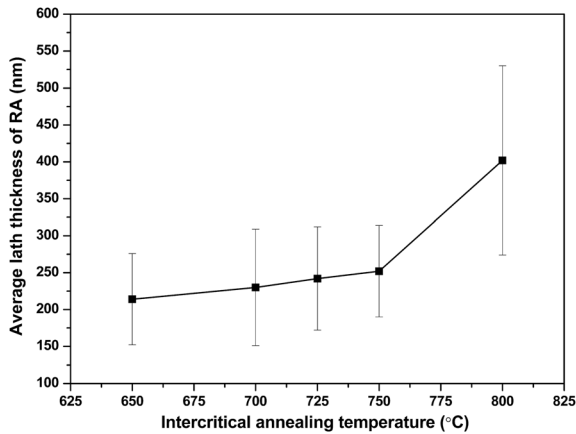


Fig. 3 Variations in RA size (lath thickness) with different IA temperatures

apparatus using an alcohol solution with 5 vol.% perchloric acid at -20°C . TEM micrographs with a magnification of $20,000\times$ were used to measure the RA thickness, and the RA thickness results were the average of at least 100 laths. Auger electron spectroscopy (AES) was applied for electron backscatter diffraction (EBSD) measurements utilizing a PHI 710

microprobe operating at 20 kV with a step size of $0.04\ \mu\text{m}$. The EBSD samples were electropolished in the same solution as that for the TEM thin foils. The RA volume fraction was measured via x-ray diffraction (XRD) using a Cu-K α radiation source operating at 150 mA and 40 kV. The integrated intensities of the $(200)_{\alpha}$, $(211)_{\alpha}$, $(200)_{\gamma}$, $(220)_{\gamma}$ and $(311)_{\gamma}$ diffraction peaks were used for the calculations. The carbon content in the RA was calculated using the following modified empirical equation (Ref 25):

$$a_{\gamma} = 3.556 + 0.0453X_{\text{C}} + 0.00095X_{\text{Mn}} + 0.0056X_{\text{Al}} \quad (\text{Eq 1})$$

where X_{C} , X_{Mn} and X_{Al} (wt.%) are the C, Mn and Al contents in RA, respectively; a_{γ} (\AA) is the austenite lattice parameter. The measured value of X_{Mn} through EDS analysis of at least 10 randomly selected phases was adopted in this calculation. $X_{\text{Al}} = 2.69$ for it has been verified that the Al content is insensitive to T_{IA} (Ref 8).

Specimens for tensile testing were machined along the rolling direction to a 2 mm thickness, 5 mm width and 25 mm gauge length. Tensile tests were conducted on a testing machine at a crosshead speed of 1 mm/min. The fracture surfaces of fractured tensile specimens were observed by SEM.

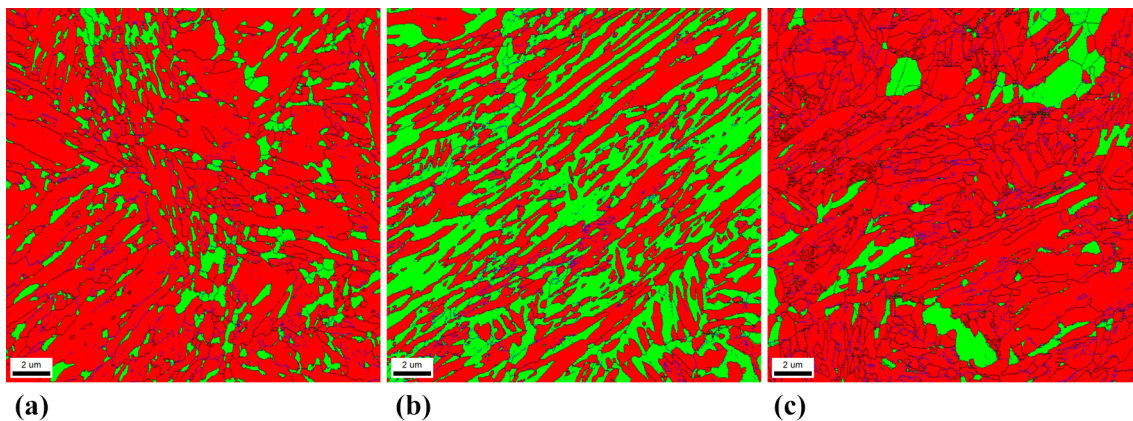


Fig. 4 EBSD micrographs of the (a) HR650, (b) HR725 and (c) HR800 samples. Green color refers to RA, and red color refers to ferrite matrix (Color figure online)

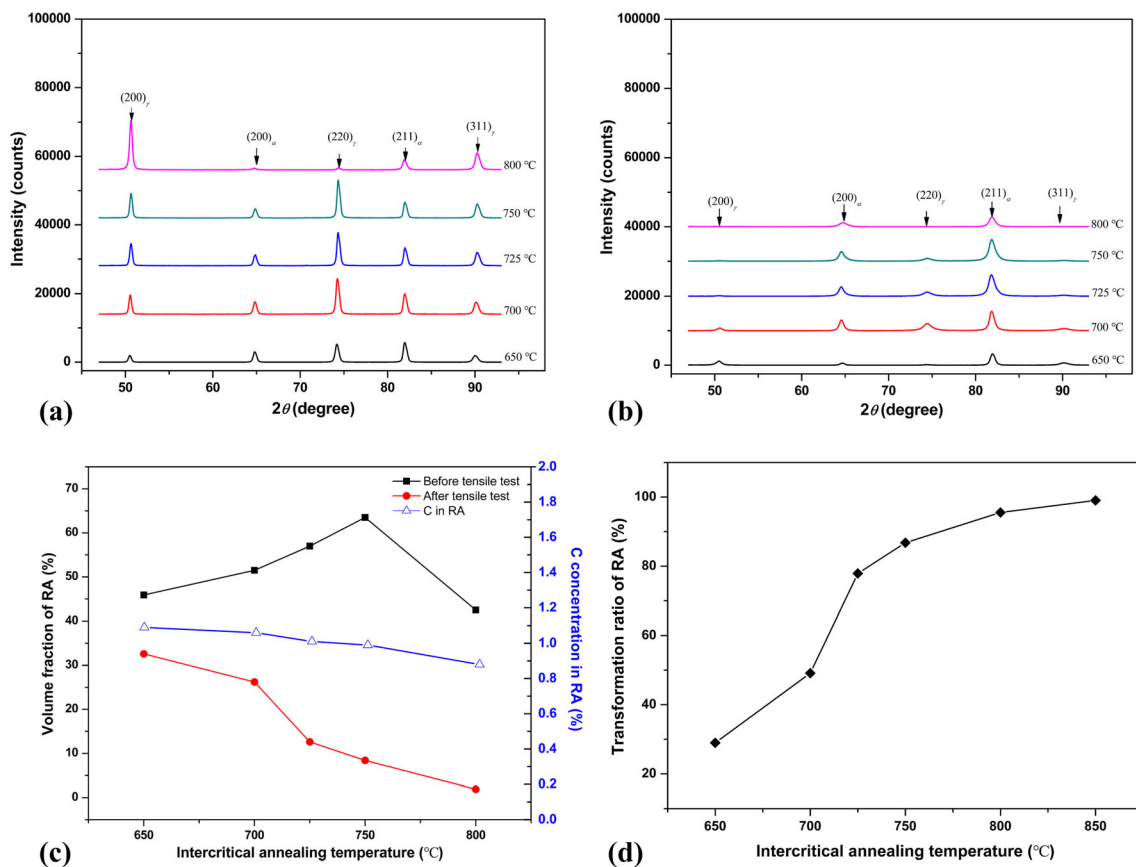


Fig. 5 (a) XRD patterns before tensile test; (b) XRD patterns after tensile test; (c) the measured RA fraction and the C content in the RA; (d) the transformation ratio of RA

3. Results

3.1 Microstructure Characteristics

Figure 1(a), (b), (c) and 2 presents the SEM and TEM micrographs of the samples intercritically annealed at different temperatures. The SEM microstructure of the HR650 sample is somewhat similar to that of high-temperature tempered martensite with a considerable number of cementite particles although

a lamellar type ultrafine duplex microstructure consisting of lathy austenite and emerging ferrite phase (Fig. 2a). It is obvious that the amount of cementite particles significantly decreases with an increase in T_{IA} . This could be further confirmed by the changes of phase volume fractions with temperature predicted by the Thermo-Calc software as shown in Fig. 1(d), which reveals that the dissolving temperature of cementite is ~ 650 °C. The average RA lath thickness obtained from TEM micrographs increases slightly with an increase in

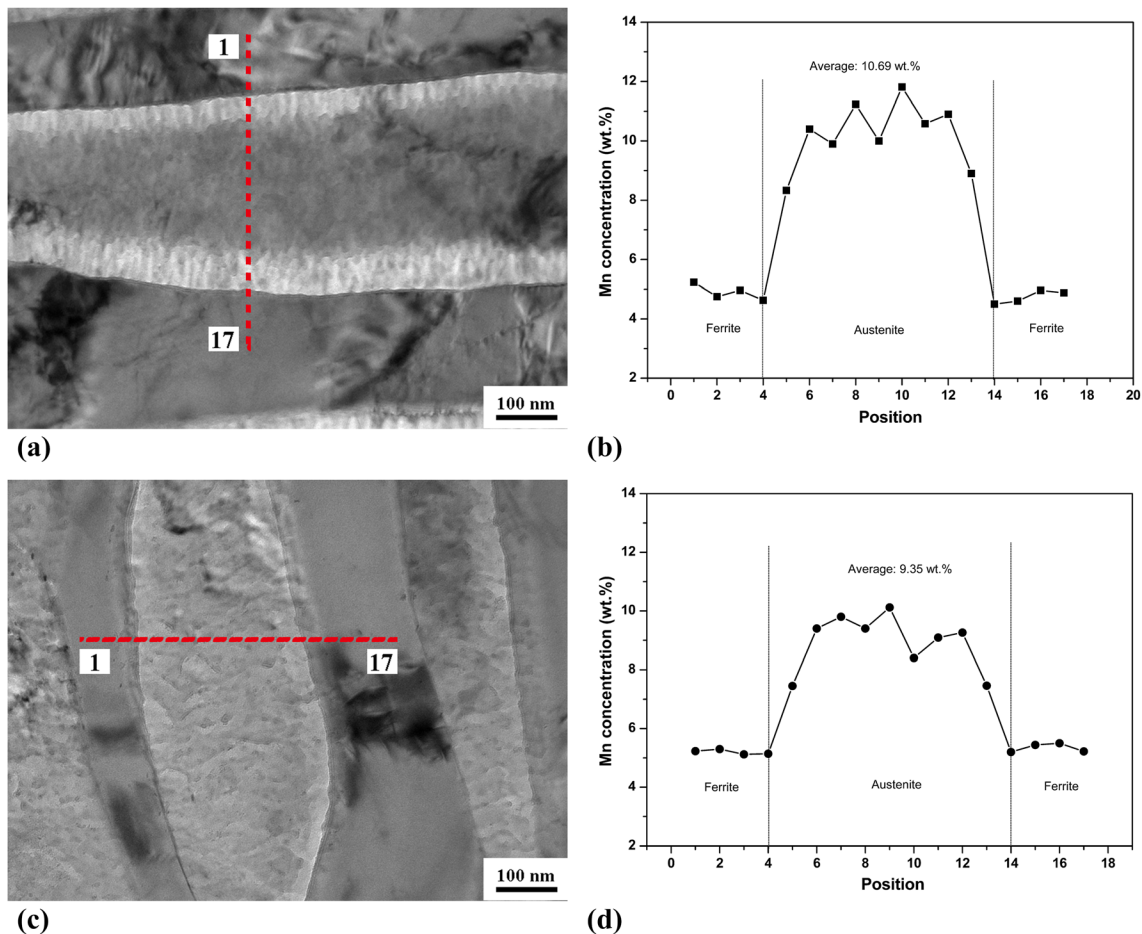


Fig. 6 TEM-EDS analysis showing the partition of Mn between the ferrite and austenite in the microstructure after intercritically annealed at (a, b) 650 °C and (c, d) 725 °C

T_{IA} at first and then increases remarkably when T_{IA} is higher than 750 °C as shown in Fig. 3. Figure 4 also clearly shows the microstructural evolution of the HR650, HR725 and HR800 samples examined by EBSD. It can be seen that both the volume fraction and size of RA increase with an increase in T_{IA} from 650 to 725 °C, and then the volume fraction of RA decreases sharply when T_{IA} was increased up to 800 °C.

Figure 5 shows the XRD diffractogram and the measured RA fractions of the samples before and after tensile tests. The RA fraction before tensile test increases with increasing T_{IA} at first, reaching a peak value of ~ 65 vol.% at 750 °C, and then notably decreases at higher temperatures, while the RA fraction after tensile test decreases monotonically with an increase in T_{IA} , and thus causes a steep increase in the RA transformation ratio with an increase in T_{IA} . This increase–decrease pattern of the RA fraction with T_{IA} has been confirmed by many researchers (Ref 3, 6, 8). As shown in Fig. 5(c), the C content in the RA decreases with an increase in T_{IA} . The TEM micrographs and corresponding EDS analysis of the HR650 and HR725 samples are shown in Fig. 6. The average Mn content in the RA also decreases with an increase in T_{IA} . Similar results were also found in other medium-Mn steels and were further verified by the predictions using the Thermo-Calc software (Ref 6, 8, 11, 15). Notably, the RA fraction of the HR800 sample in Fig. 4(c) is much lower than that obtained from the XRD, which is probably because of the transformation

of part RA into martensite during the preparation of the sample because of the rather low stability of the RA at this condition. Moreover, it has been confirmed that the RA fraction measured by EBSD is usually lower than that measured by XRD. This difference is mainly due to the difference in analysis volume effect, i.e., EBSD is area analysis, while XRD is volume analysis (Ref 10).

3.2 Tensile Properties

Figure 7 shows the engineering stress–strain curves and the dependence of tensile properties on T_{IA} of the tested steel. It is obvious that the tensile behavior was clearly influenced by the change of T_{IA} . All the stress–strain curves exhibit continuous and smooth yielding behavior with no localization except for the samples intercritically annealed at 775 and 800 °C (Fig. 7a). The stress–strain curves also exhibit noticeable serrated or jerk flow features for the samples intercritically annealed at 725, 750, 775 and 800 °C. Such serrated flow curve was often found in medium-Mn and TWIP steels as will be discussed in section 4.2. Figure 7(b) shows that the UTS decreases slightly with an increase in T_{IA} up to 700 °C and then increases significantly with further increasing T_{IA} , while the yield strength (YS) decreases monotonically with an increase in T_{IA} . The TEL increases with increasing T_{IA} at first, reaching a maximum at 725 °C, and then decreases with further increasing T_{IA} as shown in Fig. 7(c). As a result, the UTS × TEL reaches

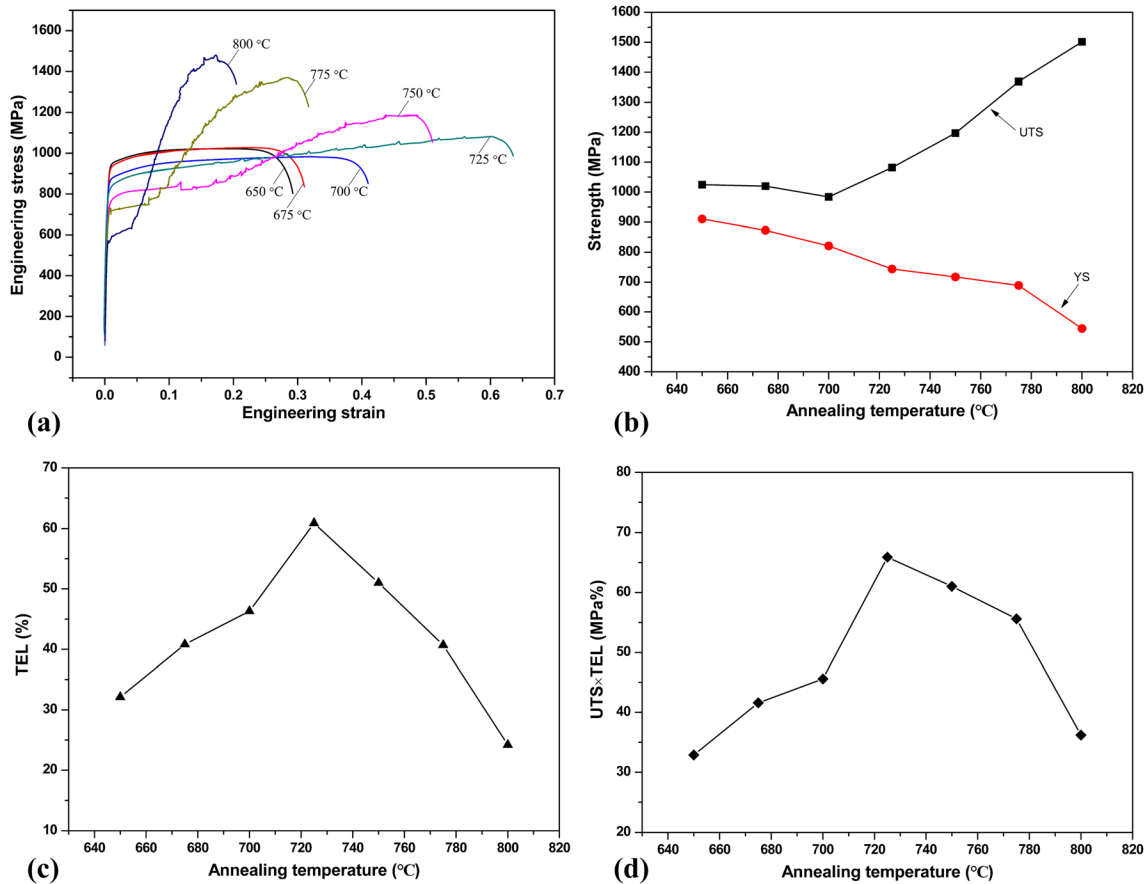


Fig. 7 (a) Engineering stress–strain curves and (b, c, d) variations of tensile properties with IA temperature. (a) Engineering stress–strain curves; (b) UTS and YS; (c) TEL; (d) UTS \times TEL

a maximum at 725 °C (Fig. 7d). This T_{IA} dependence of the tensile properties is common to most medium-Mn steels in the literature (Ref 3, 6, 7, 11, 19, 21, 22, 26).

3.3 Fractography

Figure 8 and 9 presents the fracture appearances of the intercritically annealed samples after tensile testing. Two distinct macroscopic regions of fracture surfaces were found present. The first region is smooth, while the second region contains delaminations, in which crack branched in the longitudinal direction of the samples. The HR725 sample shows the most serious delamination, while the HR800 sample exhibits negligible delamination. The tensile fracture surface of the HR650 sample exhibits a mixed mode fracture of ductile dimples and quasi-cleavage facets with a few micro-delamination cracks (Fig. 9a), reflecting enhanced ductility (TEL = 32.1%, Fig. 7c) after IA at 650 °C. For the HR700 sample, the fracture surface in the smooth region reveals predominately transgranular fracture with many micro-delamination cracks (indicated by white arrows) as shown in Fig. 9(b). The fracture surfaces in the smooth regions of the HR725 and HR800 samples are also characterized primarily by quasi-cleavage fracture with many micro-delamination cracks as shown in Fig. 9(c) and (d). Both the size and number of the micro-delamination cracks tend to increase with increasing T_{IA} . The fracture surface in the delamination cracks region is characterized by primarily ductile dimples for the HR700 and HR725 samples (Fig. 9e), while it is mainly quasi-cleavage for the

HR800 sample (Fig. 9f), reflecting decreased ductility of the latter.

4. Discussion

4.1 Mechanical Properties

There are different variations of the UTS, YS and TEL with increasing T_{IA} , i.e., the UTS and YS diverge with an increase in T_{IA} , while the TEL reaches a maximum value at an intermediate T_{IA} as shown in Fig. 7. Similar variations in mechanical properties with T_{IA} were also observed in previous studies of other medium-Mn steels (Ref 6, 11, 27). Interestingly, as shown in Table 2, the tested hot-rolled medium-Mn steel exhibits superior UTS \times TEL compared to those reported for other hot- and cold-rolled medium-Mn steels with similar Mn contents (Ref 10, 15, 28-30), which is also much higher than the target UTS \times TEL for the third-generation AHSSs and is even comparable to those of the twinning-induced plasticity (TWIP) steels (Ref 2-5). Such excellent UTS \times TEL is regarded to be mainly attributed to the microstructural characteristics and the corresponding TRIP effect taking place during tensile deformation as will be discussed later.

As the microstructure of the tested samples is a mixture of ferrite, RA and/or cementite and martensite, the tensile flow stress can be predicted using the rule of mixture for multiphase steels (Ref 31). Thus, the UTS is mainly related to the volume

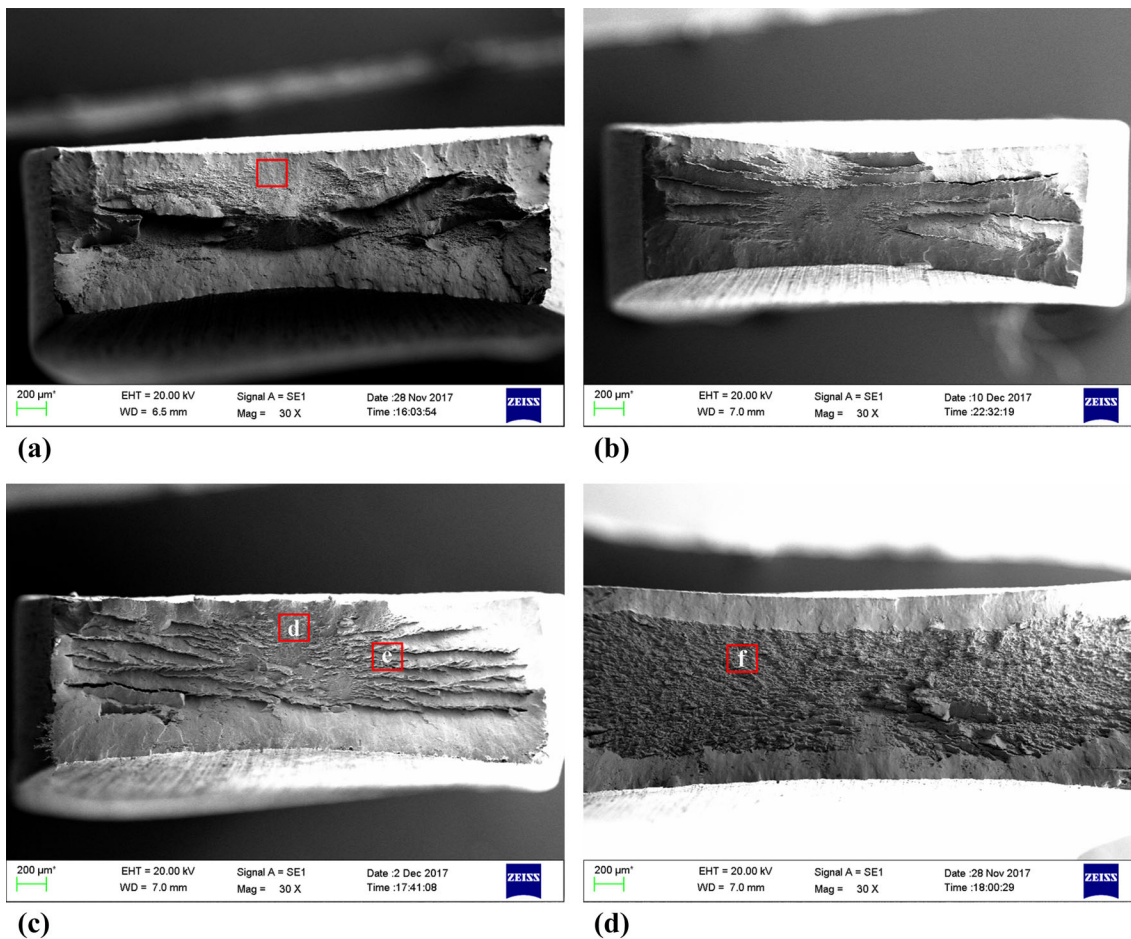


Fig. 8 SEM micrographs showing the tensile fracture appearances of the (a) HR650, (b) HR700, (c) HR725 and (d) HR800 samples

fractions of original constituent phases and the deformation-induced martensite (DIM) during tensile deformation (Ref 32). As shown in Fig. 5, both the RA fraction before tensile testing and the DIM fraction (the difference between the RA fractions before and after tensile testing) increase with increasing T_{IA} up to 700 °C which are beneficial to enhance the UTS. However, the dissolution of the cementite particles and the softening of the initial martensitic matrix in the as-hot-rolled condition with increasing T_{IA} tend to lower the UTS. As a result, the UTS decreases slightly with increasing T_{IA} up to 700 °C because the softening effect prevailed over the hardening effect, and then increases with further increasing T_{IA} mainly because of the notably increased RA and DIM fractions (Fig. 5c and d). The TEL increases with increasing T_{IA} up to 725 °C due to the TRIP effect. However, when the sample was intercritically annealed at temperatures above 750 °C, the RA transformed at an early stage of deformation due to its reduced stability as will be discussed in the next section. This caused a decrease in the TEL with further increasing T_{IA} . The increasing amount of total martensite (the DIM formed during tensile deformation and the martensite formed during cooling after IA due to the decreased RA stability) tends to play a major role, and then the UTS still increases with further increasing T_{IA} higher than 750 °C. It should be noted that the TWIP effect might be another factor that contributes to the high TEL of the tested medium-Mn steel because it was reported that the TWIP + TRIP effects occurred during tensile deformation in Al-containing medium-Mn steels

with higher Mn contents (Ref 20); thus, further research is required to clarify this issue.

As noticeable plastic deformation of one phase with considerable fraction and reasonable distribution would cause the deformation of the overall material, it is thus considered that the YS of multiphase steel depends primarily on the deformation of the softest phase (Ref 32). As the hardness of RA phase is lower than those of intercritical ferrite (IF) and martensite in medium-Mn steels (Ref 9, 33), it is reasonable to suggest that the RA is the first constituent to deform plastically before the yielding of the IF. The relationship between the YS and the inverse square root of the RA lath thickness obeys the Hall-Petch relation as shown in Fig. 10, although this relation is basically more applicable to single phase metals and alloys (Ref 34). Similar results were also reported by other researchers (Ref 6, 35, 36). Therefore, it is suggested that the YS of the tested steel depends primarily on the RA lath thickness. In addition, it is also suggested that the greater degree of softening of the initial martensitic matrix with increasing T_{IA} also contributes to this variation.

4.2 Austenite Stability and Work Hardening Behavior

As shown in Fig. 5(d), there is a notable increase in the transformation ratio of RA with increasing T_{IA} , which suggests that the RA stability is significantly lowered with increasing T_{IA} . This could be further confirmed by the increasing of the RA size (Fig. 3) and the decreasing of the C and Mn contents in

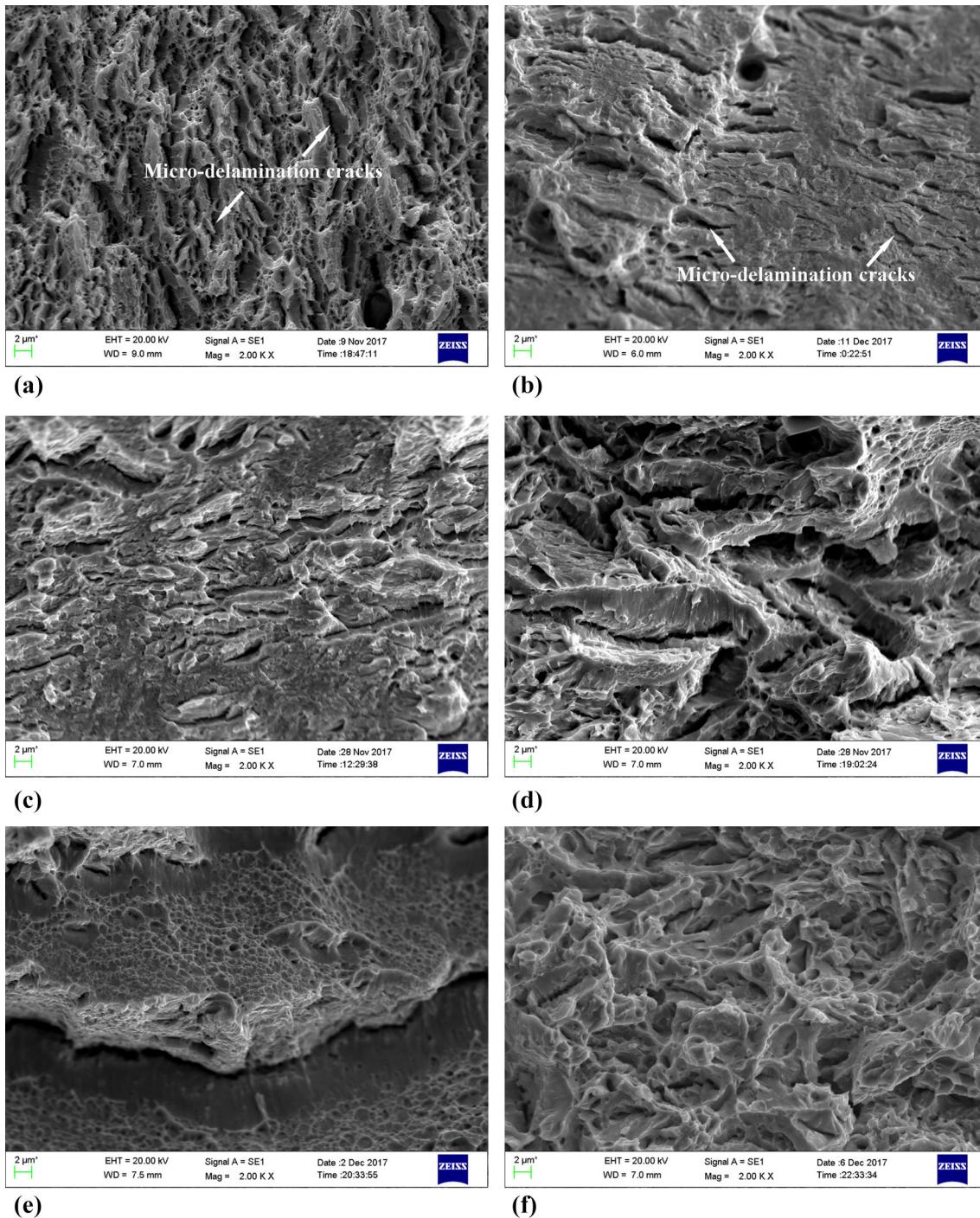


Fig. 9 SEM micrographs of the fracture surfaces of the (a) HR650, (b) HR700, (c, e) HR725 and (d, f) HR800 samples

the RA with increasing T_{IA} (Fig. 5c and 6). It is regarded that both the RA size and the contents of strong austenite stabilizing elements of C and Mn in RA have a significant influence on the stability of RA (Ref 6, 11, 22). Moreover, the change of the morphology of the RA with increasing T_{IA} (Fig. 4) also would affect its stability (Ref 37).

Given that work hardening (WH) is expected to be affected by the stability of the RA, the WH rate–true strain curves and the true stress–true strain curves of the tested samples are presented in Fig. 11. The WH behavior can be roughly divided into three stages. The WH rate decreases sharply at the

beginning stage of deformation in stage 1 for all the samples, and it is regarded that this stage is mainly connected with the deformation of ferrite (Ref 38) or most probably due to the fast dynamic recovery (Ref 7). For the HR650 sample, its WH rate shows a gradual decrease with increasing true strain in stage 2, as was also observed by other researchers (Ref 6, 22). Its value of WH rate is the lowest among all the samples, suggesting limited contribution of deformation-induced transformation of austenite into martensite (DIM) as shown in Fig. 5, and thus, its $UTS \times TEL$ is accordingly the lowest (Fig. 7d).

Table 2 Comparisons of the mechanical properties of the tested medium-Mn steel with those of others with similar Mn contents in the literature

Composition	Heat treatment	UTS, MPa	TEL, %	UTS × TEL, GPa%	References
0.4C-8Mn-2Si-3Al-0.2V	HR + IA	1200	40	48	Ref 28
0.23C-8.1Mn-5.3Al	CR + IA	949	54	51	Ref 29
0.2C-8.5Mn-3Al	HR + QT	1110	35	38	Ref 30
0.2C-8.5Mn-1.5Al	HR + QT	1373	32	44	Ref 30
0.2C-8Mn-4Al	HR + QT	987	33	33	Ref 15
0.05C-8.5Mn-0.3Si	HR + IA	1034	27	28	Ref 10
0.05C-8.5Mn-0.3Si	CR + IA	1193	25	30	Ref 10
0.25C-8.5Mn-0.5Si-2.5Al	HR + IA	1082	61	66	Present work

HR—hot-rolled, CR—cold-rolled, IA—intercritical annealing, QT—quenching at intercritical temperature and tempering at 200 °C.

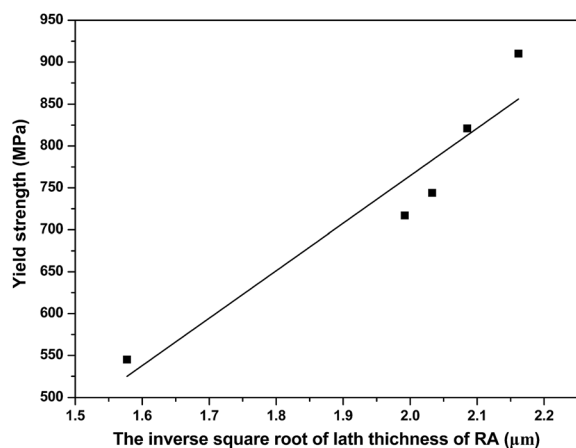


Fig. 10 Relationship between the YS and the RA lath thickness of the samples intercritically annealed at different temperatures

In the case of samples intercritically annealed at temperatures higher than 650 °C, stage 2 is characterized by a relatively steady state, while stage 3 is characterized by a significant fluctuation of WH rate with increasing T_{IA} . It is regarded that stage 2 is a consequence of the TRIP effect accompanied by the cooperative deformation of ferrite (Ref 6, 22). The competition between the softening effect of ferrite and the hardening contribution of the TRIP effect causes the decrease or increase in the WH rate. By the way, it is also suggested that some initial strain is necessary to develop sufficient martensite nucleation sites, and once these sites are formed, the austenite-to-martensite transformation would occur readily, thus contributing to the enhanced WH rate (Ref 11).

Significant fluctuation of WH rate in stage 3 is ascribed to the discontinuous TRIP effect which is primarily due to the presence of RA with different degrees of stability as well as the relaxation and transfer of local stress owing to martensite transformation (Ref 8, 9). The occurring of the discontinuous TRIP effect contributes to additional enhancing of strength and ductility. Figure 12 shows the variations of the critical strain (ϵ_c) for the massive initiation of discontinuous TRIP effect, the additional strain caused by discontinuous TRIP effect (ϵ_{dis}) and the total strain (ϵ_{total}) with T_{IA} . It is obvious that ϵ_c decreases monotonically, while ϵ_{dis} increases at first and then decreases with increasing T_{IA} , and thus causes a peak value of ϵ_{total} at

725 °C. As the general stability of the RA decreases with increasing T_{IA} , it is inferred that ϵ_c depends mainly on the stability of the RA as well as the cooperative deformation of the ferrite, while ϵ_{dis} depends mainly on both the stability and the stability range of the RA. Obviously, ϵ_{dis} decreases with the increase in the intensity of discontinuous TRIP effect when comparing Fig. 11(c), (d), (e) and (f). Moreover, the average value of WH rate in stage 3 generally increases with increasing T_{IA} , indicating an increasing DIM transformation as revealed in Fig. 5(d).

It is interesting to note that when T_{IA} is low, such as being lower than 700 °C, the RA is too stable to cause large TRIP effect and correspondingly little effect on WH, whereas when T_{IA} is too high, such as being higher than 750 °C, the RA is too unstable and thus causes an early and fast discontinuous austenite-to-martensite transformation and correspondingly rapid WH. To confirm this assumption, the HR650, HR725 and HR800 samples were pre-strained to about 0.10 and the remaining RA volume fractions were examined by XRD. The result shows that the transformation ratio of RA is 3.3, 19.2 and 98.8% for the HR650, HR725 and HR800 samples, respectively, i.e., the tested steel displayed progressively decreasing RA stability with increasing T_{IA} . It is worth pointing out that a pre-straining of 0.10 corresponds to the mid-term of stage 2 for the HR725 sample (Fig. 11c), while it corresponds to the nearly finishing state of stage 3 for the HR800 sample (Fig. 11f). It is obvious that most of the austenite-to-martensite transformation occurred at strain well above 0.10 for the HR725 sample, while the austenite-to-martensite transformation almost finished at strain even below 0.10 for the HR800 sample. Therefore, it is suggested that optimal UTS × TEL could be obtained when the RA has both suitable stability and large stability range.

4.3 Fracture and Void Initiation Characteristics

As shown in the tensile specimen fracture surfaces of the tested samples (Fig. 8 and 9), distinct macro- and micro-delaminations were found for the samples intercritically annealed at temperatures of 700 and 725 °C. The distance between neighboring micro-cracks is about 2-5 μm, which is much wider than the width of the RA or ferrite (about 0.2-0.4 μm) as shown in Fig. 2 and 3. Similar delamination fracture was also reported in an ultrafine elongated grain structure of tempered martensite steel (Ref 39) and a lamellar structured ultrafine grain dual-phase steel (Ref 40). Sun et al. (Ref 40) regarded that this delamination fracture is mainly associated with the texture which caused strength differences between the

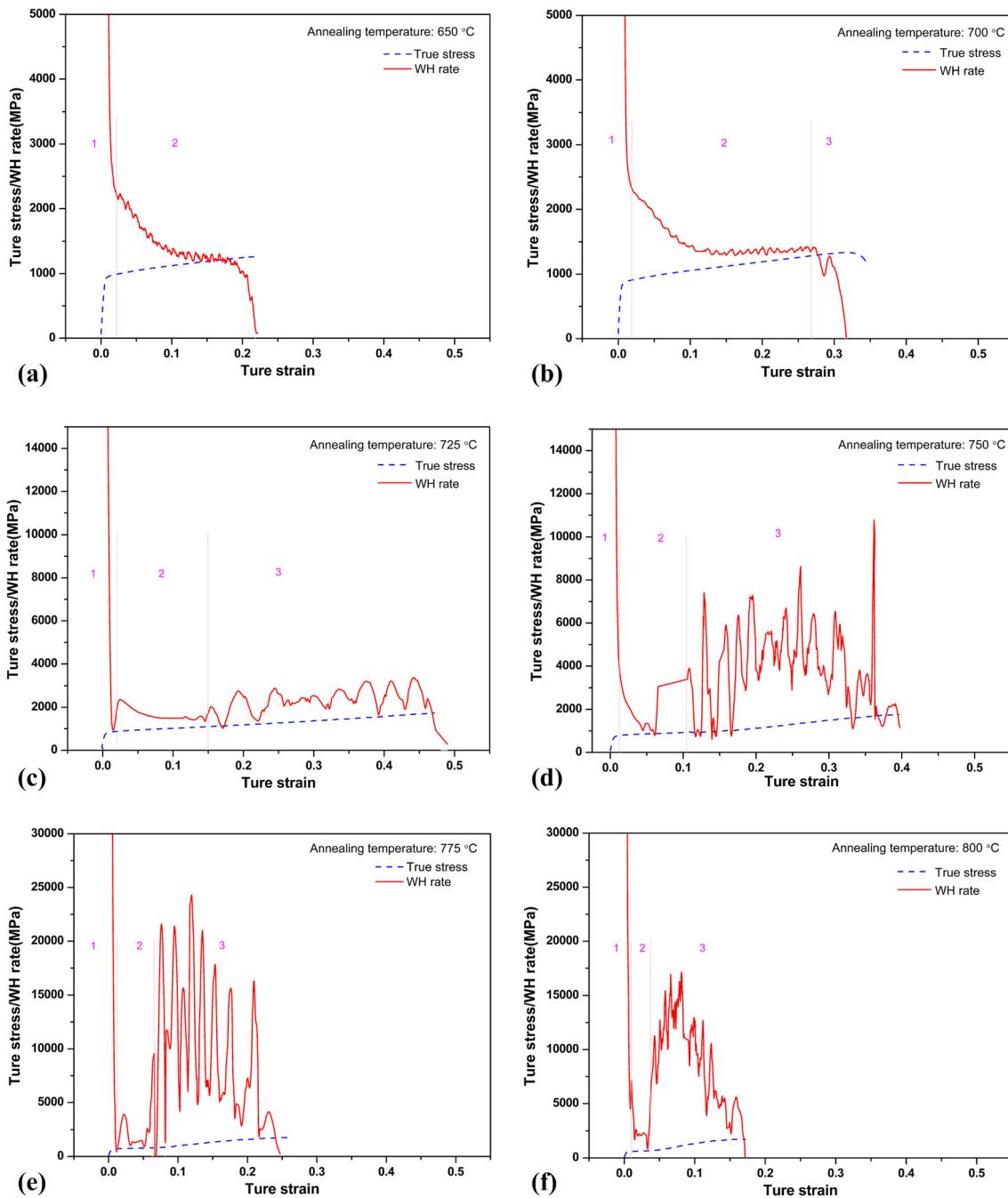


Fig. 11 True stress–true strain curves and work hardening (WH) rate–true strain curves of the of samples intercritically annealed at (a) 650 °C, (b) 700 °C, (c) 725 °C, (d) 750 °C, (e) 775 °C and (f) 800 °C

longitudinal and transverse directions. It was found that the RA grains in a hot-rolled medium-Mn steel (0.3C-6.0Mn-3Al-1.5Si) had mainly the Brass and Cu texture as part of α -fiber and τ -fiber orientations, respectively (Ref 33). Our recent study (Ref 41) suggested that this delamination fracture is primarily associated with the microstructural anisotropy causing strength differences in a heavy warm-rolled Al-containing medium-Mn steel with well-developed lamellar structure. Nevertheless, further systematic study is needed to clarify this issue.

During tensile deformation, it is known that the RA transforms gradually to martensite and causes the so-called TRIP effect. As the C content in the RA is rather high (Fig. 5c),

the strength level of the martensite is thus much higher than that of the soft ferrite, i.e., these two phases exhibit rather different deformation characteristics. Therefore, the martensite did not deform significantly while the ferrite deformed plastically during deformation, which caused large strain gradient building up at the ferrite/martensite interface, and thus voids formed at that interface (Ref 33, 42, 43). Figure 13 presents the SEM micrographs showing voids that nucleated at the ferrite/martensite interfaces. As the RA was too stable, only fraction of RA transformed to martensite during tensile deformation, and thus, only a few micro-delamination cracks were observed for the HR650 sample (Fig. 9a). When T_{1A} was increased higher than

650 °C, more volume fractions of the RA transformed to martensite and thus resulted in an increase in the TEL and the amount of micro-delamination cracks, although their fracture surfaces were characterized by a mixture of quasi-cleavage and dimple fractures. It is obvious that well-developed micro-delamination cracks were observed for the HR800 sample; this is because the RA was too unstable and thus caused an early martensite transformation during tensile deformation. Moreover, the pre-existing martensite in the high-temperature annealed sample also contributed to the early formation and growth of micro-delamination cracks.

5. Conclusions

- (1) An ultrafine duplex lamellar microstructure primarily consisting of RA and recrystallized ferrite was obtained under given IA conditions. A volume fraction of RA as high as 65 vol.% was obtained at T_{IA} of 750 °C, and the lath thickness of RA increases with increasing T_{IA} .
- (2) The UTS decreases slightly and then increases, while the YS decreases with increasing T_{IA} , and the TEL and

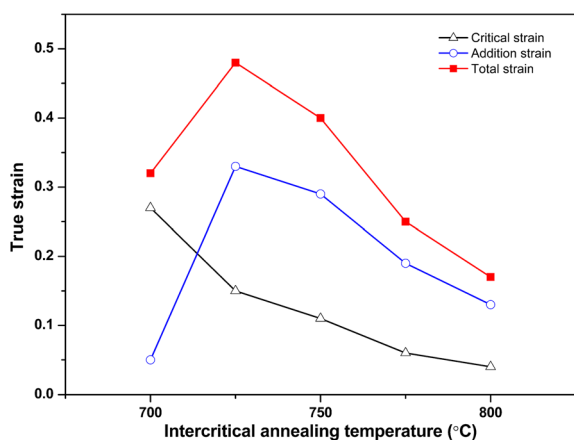


Fig. 12 Variations of the critical strain for the initiation of discontinuous TRIP effect, the additional strain caused by discontinuous TRIP effect and the total strain with IA temperature

UTS \times TEL exhibit increase–decrease patterns with T_{IA} . A maximum value of UTS \times TEL of 66 GPa% was obtained at T_{IA} of 725 °C, which is notably superior to those of previously investigated medium-Mn steels with similar Mn contents.

- (3) Both the RA size and the contents of strong stabilizing elements of C and Mn in the RA significantly influence the stability of the RA. It is found that the critical strain for the massive initiation of discontinuous TRIP effect decreases, while the additional strain caused by discontinuous TRIP effect increases at first and then decreases with increasing T_{IA} . Therefore, it is suggested that optimal combination of strength and ductility could be obtained when the RA has suitable stability range besides comparatively high amount.
- (4) The tensile fracture mechanism changes with the variation of T_{IA} . The fracture is primarily a mixed mode fracture of ductile dimples and quasi-cleavage facets at T_{IA} of 650 °C, and then it is predominately transgranular fracture with many micro-delamination cracks accompanied with many fine ductile dimples at T_{IA} of 700 and 725 °C. This kind of micro-delamination fracture, which was found to be primarily nucleated and propagated at the interface of transformation-induced martensite and ferrite, became more significant with increasing T_{IA} .

Acknowledgments

This work was supported by the Fundamental Research Funds for the Central Universities (No. 2017RC024).

References

1. M. Takahashi, Sheet Steel Technology for the Last 100 Years: Progress in Sheet Steels in Hand with the Automobile Industry, *ISIJ Int.*, 2015, **55**, p 79–88
2. D.W. Suh and S.J. Kim, Medium Mn Transformation-Induced Plasticity Steels: Recent Progress and Challenges, *Scr. Mater.*, 2017, **126**, p 63–67
3. Y.K. Lee and J. Han, Current Opinion in Medium Manganese Steel, *Mater. Sci. Technol.*, 2015, **31**, p 843–856

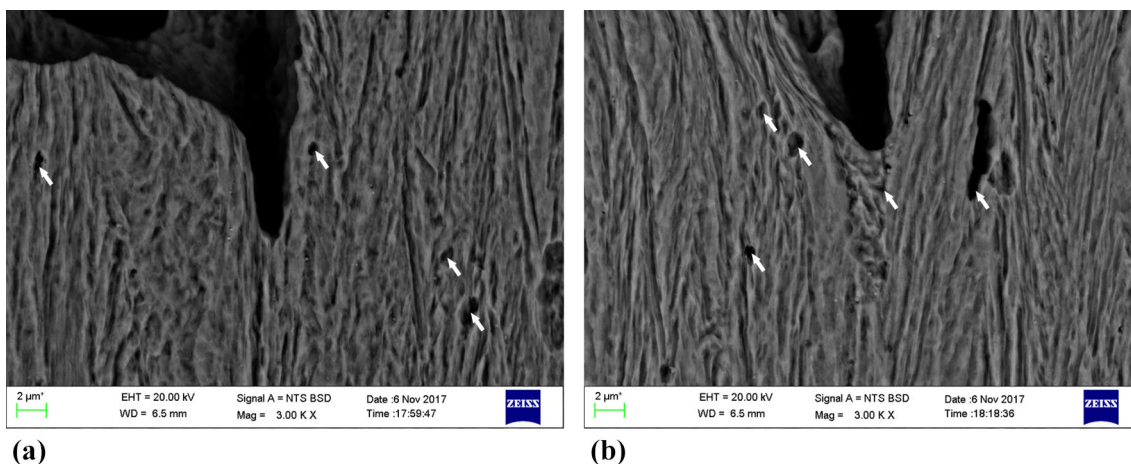


Fig. 13 SEM micrographs of the microstructure of the HR725 sample after tensile deformation

4. H. Dong, W.Q. Cao, J. Shi, C.Y. Wang, M.Q. Wang, and Y.Q. Weng, Microstructure and Performance Control Technology of the 3rd Generation Auto Sheet Steels, *Iron Steel*, 2011, **46**(6), p 1–11
5. E. De Moor, P.J. Gibbs, J.G. Speer, D.K. Matlock, and J. Schroth, Strategies for Third-Generation Advanced High-Strength Steel Development, *Iron Steel Technol.*, 2010, **7**, p 133–144
6. C.W. Shao, W.J. Hui, Y.J. Zhang, X.L. Zhao, and Y.Q. Weng, Microstructure and Mechanical Properties of Hot-Rolled Medium-Mn Steel Containing 3% Aluminum, *Mater. Sci. Eng., A*, 2017, **682**, p 45–53
7. S.J. Lee, S.M. Shin, M.Y. Kwon, K.Y. Lee, and B.C. De Cooman, Tensile Properties of Medium Mn Steel with a Bimodal UFG $\alpha + \gamma$ and Coarse δ -Ferrite Microstructure, *Metall. Mater. Trans. A*, 2017, **48**, p 1678–1700
8. Z.C. Li, H. Ding, R.D.K. Misra, Z.H. Cai, and H.X. Li, Microstructural Evolution and Deformation Behavior in the Fe-(6,8.5)Mn-3Al-0.2C TRIP Steels, *Mater. Sci. Eng., A*, 2016, **672**, p 161–169
9. Z.H. Cai, H. Ding, H. Kamoutsi, G.N. Haidemenopoulos, and R.D.K. Misra, Interplay Between Deformation Behavior and Mechanical Properties of Intercritically Annealed and Tempered Medium-Manganese Transformation-Induced Plasticity Steel, *Mater. Sci. Eng., A*, 2016, **654**, p 359–367
10. J. Han, S.J. Lee, J.G. Jung, and Y.K. Lee, The Effects of the Initial Martensite Microstructure on the Microstructure and Tensile Properties of Intercritically Annealed Fe-9Mn-0.05C Steel, *Acta Mater.*, 2014, **78**, p 369–377
11. P.J. Gibbs, E. De Moor, M.J. Merwin, B. Clausen, J.G. Speer, and D.K. Matlock, Austenite Stability Effects on Tensile Behavior of Manganese-Enriched-Austenite Transformation-Induced Plasticity Steel, *Metall. Mater. Trans. A*, 2011, **42**, p 3691–3702
12. C. Wang, J. Shi, C.Y. Wang, W.J. Hui, M.Q. Wang, H. Dong, and W.Q. Cao, Development of Ultrafine Lamellar Ferrite and Austenite Duplex Structure in 0.2C5Mn Steel During ART-Annealing, *ISIJ Int.*, 2011, **51**, p 651–656
13. B. Hu, H.W. Luo, F. Yang, and H. Dong, Recent Progress in Medium-Mn Steels Made with New Designing Strategies, a Review, *J. Mater. Sci. Technol.*, 2017, **33**, p 1457–1464
14. M.H. Cai, H.S. Huang, J.H. Su, H. Ding, and P.D. Hodgson, Enhanced Tensile Properties of a Reversion Annealed 6.5Mn-TRIP Alloy via Tailoring Initial Microstructure and Cold Rolling Reduction, *J. Mater. Sci. Technol.*, 2018, **34**(8), p 1428–1435
15. Z.H. Cai, H. Ding, Z.Y. Ying, and R.D.K. Misra, Microstructural Evolution and Deformation Behavior of a Hot-Rolled and Heat-Treated Fe-8Mn-4Al-0.2C Steel, *J. Mater. Eng. Perform.*, 2014, **23**, p 1131–1137
16. S.J. Lee, S.W. Lee, and B.C. De Cooman, Mn Partitioning During the Intercritical Annealing of Ultrafine-Grained 6% Mn Transformation-Induced Plasticity Steel, *Scr. Mater.*, 2011, **64**, p 649–652
17. X.N. Luo, X.Y. Zhong, H.W. Luo, H.H. Zhou, C.Y. Wang, and J. Shi, Mn Diffusion at Early Stage of Intercritical Annealing of 5Mn Steel, *J. Iron Steel Res. Inter.*, 2015, **22**, p 1015–1019
18. R.L. Miller, Ultrafine-Grained Microstructures and Mechanical Properties of Alloy Steels, *Metall. Trans. A*, 1972, **3**, p 905–912
19. M.J. Merwin, Low-Carbon Manganese TRIP Steels, *Mater. Sci. Forum*, 2007, **539–543**, p 4327–4332
20. B. Hu and H.W. Luo, A Strong and Ductile 7Mn Steel Manufactured by Warm Rolling and Exhibiting Both Transformation and Twinning Induced Plasticity, *J. Alloy. Compd.*, 2017, **725**, p 684–693
21. D.W. Suh, S.J. Park, T.H. Lee, C.S. Oh, and S.J. Kim, Influence of Al on the Microstructural Evolution and Mechanical Behavior of Low-Carbon, Manganese Transformation-Induced-Plasticity Steel, *Metall. Mater. Trans. A*, 2010, **41**, p 397–408
22. Z.H. Cai, H. Ding, R.D.K. Misra, and Z.Y. Ying, Austenite Stability and Deformation Behavior in a Cold-Rolled Transformation-Induced Plasticity Steel with Medium Manganese Content, *Acta Mater.*, 2015, **84**, p 229–236
23. I. Gutierrez-Urrutia and D. Raabe, Influence of Al Content and Precipitation State on the Mechanical Behavior of Austenitic High-Mn Low-Density Steels, *Scr. Mater.*, 2013, **68**, p 343–347
24. E. Girault, A. Mertens, P. Jacques, Y. Houbaert, B. Verlinden, and J.V. Humbeeck, Comparison of the Effects of Silicon and Aluminium on the Tensile Behaviour of Multiphase TRIP-Assisted Steels, *Scr. Mater.*, 2001, **44**, p 885–892
25. N.H. van Dijk, A.M. Butt, L. Zhao, J. Sietsma, S.E. Offerman, J.P. Wright, and S. van der Zwaag, Thermal Stability of Retained Austenite in TRIP Steels Studied by Synchrotron X-Ray Diffraction During Cooling, *Acta Mater.*, 2005, **53**, p 5439–5447
26. D.Y. Lee, J.K. Kim, S.W. Lee, K.Y. Lee, and B.C. De Cooman, Microstructures and Mechanical Properties of Ti and Mo Micro-alloyed Medium Mn Steel, *Mater. Sci. Eng., A*, 2017, **706**, p 1–14
27. D.W. Suh, J.H. Ryu, M.S. Joo, H.S. Yang, K. Lee, and H.K.D.H. Bhadeshia, Medium-Alloy Manganese-Rich Transformation-Induced Plasticity Steels, *Metall. Mater. Trans. A*, 2013, **44A**, p 286–293
28. S.W. Lee and B.C. De Cooman, Tensile Behavior of Intercritically Annealed Ultra-Fine Grained 8% Mn Multi-phase Steel, *Steel Res. Int.*, 2015, **86**, p 1170–1178
29. S.J. Park, B. Hwang, K.H. Lee, T.H. Lee, D.W. Suh, and H.N. Han, Microstructure and Tensile Behavior of Duplex Low-Density Steel Containing 5 Mass% Aluminum, *Scr. Mater.*, 2013, **68**, p 365–369
30. Z.C. Li, R.D.K. Misra, Z.H. Cai, H.X. Li, and H. Ding, Mechanical Properties and Deformation Behavior in Hot-Rolled 0.2C-1.5/3Al-8.5Mn-Fe TRIP Steel: The Discontinuous TRIP Effect, *Mater. Sci. Eng., A*, 2016, **673**, p 63–72
31. D. Embury and O. Bouaziz, Steel-Based Composites: Driving Forces and Classification, *Annu. Rev. Mater. Res.*, 2010, **40**, p 213–241
32. W.J. Hui, C.W. Shao, Y.J. Zhang, X.L. Zhao, and Y.Q. Weng, Microstructure and Mechanical Properties of Medium Mn Steel Containing 3%Al Processes by Warm Rolling, *Mater. Sci. Eng., A*, 2017, **707**, p 501–510
33. H.K. Choi, S.J. Lee, J.W. Lee, F. Barlat, and B.C. De Cooman, Characterization of Fracture in Medium Mn Steel, *Mater. Sci. Eng., A*, 2017, **687**, p 200–210
34. M.Y. Seok, I.C. Choi, J. Moon, S. Kim, U. Ramamurty, and J.I. Jang, Estimation of the Hall-Petch Strengthening Coefficient of Steels Through Nanoindentation, *Scr. Mater.*, 2014, **87**, p 49–52
35. R. Zhang, W.Q. Cao, Z.J. Peng, J. Shi, H. Dong, and C.X. Huang, Intercritical Rolling Induced Ultrafine Microstructure and Excellent Mechanical Properties of the Medium-Mn Steel, *Mater. Sci. Eng., A*, 2013, **583**, p 84–88
36. H.F. Xu, J. Zhao, W.Q. Cao, J. Shi, C.Y. Wang, C. Wang, J. Li, and H. Dong, Heat Treatment Effects on the Microstructure and Mechanical Properties of a Medium Manganese Steel (0.2C-5Mn), *Mater. Sci. Eng., A*, 2012, **532**, p 435–442
37. J. Chiang, B. Lawrence, J.D. Boyd, and A.K. Pilkey, Effect of Microstructure on Retained Austenite Stability and Work Hardening of TRIP Steels, *Mater. Sci. Eng., A*, 2011, **528**, p 4516–4521
38. J. Shi, X.J. Sun, W.Q. Wang, W.J. Hui, H. Dong, and W.Q. Cao, Enhanced Work-Hardening Behavior and Mechanical Properties in Ultrafine-Grained Steels with Large-Fractioned Metastable Austenite, *Scr. Mater.*, 2010, **63**, p 815–818
39. Y.H. Nie, Y. Kimura, T. Inoue, F.X. Yin, E. Akiyama, and K. Tsuzaki, Hydrogen embrittlement of a 1500-MPa tensile strength level steel with an ultrafine elongated grain structure, *Metall. Mater. Trans. A*, 2012, **43**, p 1670–1687
40. J.J. Sun, T. Jiang, Y. Sun, Y.J. Wang, and Y.N. Liu, A Lamellar Structured Ultrafine Grain Ferrite-Martensite Dual Phase Steel and its Resistance to Hydrogen Embrittlement, *J. Alloy. Compd.*, 2017, **698**, p 390–399
41. Y.J. Zhang, W.J. Hui, J.J. Wang, M. Lei, and X.L. Zhao, Enhancing the Resistance to Hydrogen Embrittlement of Al-Containing Medium-Mn Steel Through Heavy Warm Rolling, *Scr. Mater.*, 2019, **165**, p 15–19
42. Q. Tonizzo, A.F. Gourgues-Lorenzon, M. Mazière, and A. Perlade, Microstructure, Plastic Flow and Fracture Behavior of Ferrite-Austenite Duplex Low Density Medium Mn Steel, *Mater. Sci. Eng., A*, 2017, **706**, p 217–236
43. G. Avramovic-Cingara, C. Saleh, M.K. Jain, and D.S. Wilkinson, Void Nucleation and Growth in Dual-Phase Steel 600 During Uniaxial Tensile Testing, *Metall. Mater. Trans. A*, 2009, **40**, p 3117–3127

Publisher's Note Springer Nature remains neutral with regard to jurisdictional claims in published maps and institutional affiliations.